

Backscatter absorption spectroscopy for process monitoring in powder bed fusion

M. Beuting^{*1}, A. J. Fairhall², R. H. Goldsmith², L. Chen¹, S. T. Sanders¹

¹ Department of Mechanical Engineering, University of Wisconsin-Madison, Madison, USA

² Department of Chemistry, University of Wisconsin-Madison, Madison, USA

Abstract

This paper presents an optical sensor that employs backscatter tunable laser absorption spectroscopy (BTLAS) for in-situ monitoring of laser powder bed fusion (L-PBF). The measured signal depends on the conditions within the gas vapor cavity, whose dynamic interaction with the melt pool surface is known to be a major cause of defects in the final part. The sensor spectrally resolves the shape of the absorption lines of metal vapors, which is influenced by gas pressure, temperature, concentration, and velocity. This pilot study demonstrates that the absorption line strength and line shape of Ti varies significantly with changes in the process chamber pressure and laser power when processing a Ti-6Al-4V, potentially allowing the technique to be applied for process monitoring and closed-loop control. Additionally, the technique provided a signal under near-vacuum conditions, suggesting its utility for fundamental research on electron beam powder bed fusion (EB-PBF). The authors outline future steps for integrating this sensor into existing L-PBF systems for real-time operando process monitoring. Laser-induced fluorescence (LIF) was also observed during the experiments, which may provide further opportunities for in situ process monitoring.

Keywords Process monitoring, absorption spectroscopy, laser powder bed fusion, electron beam powder bed fusion, vapor plume, melt pool dynamics.

1. Introduction

Defects introduced during the powder bed fusion (PBF) process can significantly affect the quality of manufactured parts, a concern that has gained urgency as additive manufacturing enters safety-critical industries like aviation and medical devices [1,2]. Although the precise

Abbreviations: TLAS, tunable laser absorption spectroscopy; BTLAS, backscatter TLAS, LIF, laser-induced fluorescence; OES, optical emission spectroscopy

* Corresponding author.
matthias.beuting@wisc.edu
211 Engineering Research Bldg, 1500 Engineering Dr, Madison, WI 53706

28 mechanisms underlying these defects remain elusive, research has linked melt pool instabilities
29 to a range of issues, including part roughness, porosity, cracks, and mechanical performance
30 [2–4]. Consequently, real-time in situ monitoring of melt pool dynamics is crucial for operando
31 quality control and parameter adjustment [1,4]. Prior studies have suggested that only a
32 multimodal sensing approach can enhance the fidelity of process monitoring while facilitating a
33 deeper understanding of defect-forming mechanisms [4–6].

34 One of the key factors contributing to melt pool instability is the dynamic interaction between the
35 gas in the vapor cavity and melt pool, with the hot metal vapor plume exerting pressure on the
36 melt pool surface. Traditional methods for predicting print quality, such as acoustic monitoring
37 and measuring thermal emissions from the melt pool and vapor plume [7], provide only indirect
38 insights into the gas vapor conditions [3,4].

39 This paper introduces a novel optical sensor utilizing backscatter tunable laser absorption
40 spectroscopy (BTLAS). Distinct from previous methods, the sensor signal is directly influenced
41 by a variety of factors within the gas vapor cavity, including temperature, pressure, gas
42 composition, and velocity. This proof-of-principle study investigates the relationship between the
43 titanium (Ti) optical absorption signal in the vapor cavity and the processing parameters by
44 employing a near-coaxial probe laser and process laser on a Ti-6Al-4V sample. This paper also
45 provides a comprehensive outline of the subsequent steps required for designing and
46 integrating BTLAS sensors into production machines to achieve real-time monitoring
47 capabilities.

48 **2. Backscatter tunable laser absorption spectroscopy (BTLAS)**

49 **2.1. Principle**

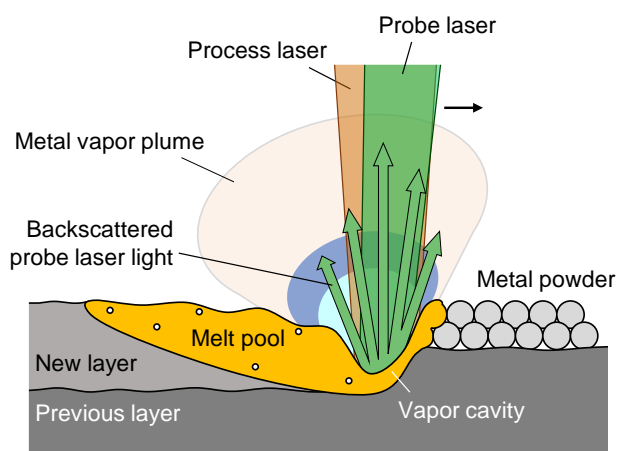
50 In both laser powder bed fusion (L-PBF) and electron beam powder bed fusion (EB-PBF), the
51 vapor plume consists of hot atomic metals found as alloying elements in the metal powder. The
52 optical properties of the vapor are characterized by the spectral lines at distinct wavelengths
53 that correspond to the electronic transitions of the individual components. The strength and
54 shape of these lines are influenced by intrinsic and extrinsic conditions of the plume such as the
55 composition, pressure, temperature, and flow velocity. In the past, spectral measurements of
56 the plume have been reported by optical emission spectroscopy (OES), in which the light
57 emitted from the metal vapor plume and the melt pool is collected and analyzed in
58 spectrometers [8,9] or using multiple detectors equipped with spectral filters [10,11]. However,
59 while the OES signal is indicative of plume composition and temperature, it provides only

60 indirect insight into parameters such as pressure and gas velocity. This information is encoded
61 in the shape and precise spectral position of the atomic lines, which typically cannot be resolved
62 by OES.

63 Recently, tunable laser absorption spectroscopy (TLAS) has been applied to EBM processes
64 [12,13]. In this method, spectral lines are probed by measuring the transmission of laser light
65 through the vapor plume. The spectral line shape can be measured by recording the
66 transmission signal while varying the probe laser wavelength. The authors recently
67 demonstrated time-resolved temperature measurements by applying TLAS directly above the
68 vapor cavity in a single-track EB-PBF experiment by rapid wavelength tuning of a vertical cavity
69 surface-emitting laser (VCSEL) [14].

70 Typically, absorption-based sensors require a line of sight between the light source and a
71 detector [15,16]. However, efforts have been made to develop single-ended sensors that can
72 detect light reflected or backscattered from rough surfaces even in harsh environments such as
73 combustion chambers and reacting flows [17–20].

74 In this paper, the authors propose a novel method for measuring the absorption within the vapor
75 cavity in powder bed fusion below the metal surface by measuring the light from a probe laser
76 backscattered from the melt pool surface, as shown in Fig. 1. Here, an input probe beam is
77 focused into the vapor cavity and the resulting backscattered TLAS (BTLAS) signal is recorded
78 after passing through the plume twice. This paves the way for a novel sensor that takes
79 advantage of the recently developed single-ended sensor approach [19] for in-situ process
80 monitoring.



81

82

Fig. 1: Backscatter absorption spectroscopy.

83 2.2. Theory

84 The attenuation of light traversing through a material is described by Beer's law (Eq. (1)) where
85 I_0 is the initial light intensity, I the intensity after passing through an absorbing medium of
86 thickness L , and S is the line strength. The number density N (particles per unit volume) is
87 proportional to the density, and for an ideal gas, it depends on the gas pressure p , temperature
88 T , and molar fraction x of the absorber. The (base-e) absorbance A is defined as the negative
89 natural logarithm of the transmission I/I_0 .

$$90 \quad -\ln\left(\frac{I}{I_0}\right) = N(T, p, x)\phi(T, p, \lambda)S(T)L = A(T, p, \lambda, x) \quad (1)$$

91 Although spectral lines arising from electronic transitions within the atoms have discrete
92 wavelengths λ , the experimentally observed absorption lines exhibit a finite width owing to
93 various line-broadening mechanisms [21]. Their influence is collectively described by the line-
94 shape function ϕ .

95 While natural broadening, owing to the uncertainty principle, is mostly negligible at elevated
96 temperatures and pressures encountered in laser processing, pressure and Doppler broadening
97 significantly affect the line shape as follows [21].

98 Pressure broadening results from particle collisions and increases with increasing gas density
99 and temperature, resulting in a Lorentzian line shape. Equation (2) describes its full width at half
100 maximum (FWHM_p), where γ is a broadening coefficient defined at a reference temperature T_{ref}
101 and n is a temperature exponent dependent on the collision partner.

$$102 \quad \text{FWHM}_p(T, p) = 2\gamma\left(\frac{T_{\text{ref}}}{T}\right)^n p \quad (2)$$

103 Doppler broadening occurs from the thermal motion of particles, causing spectral lines to
104 undergo a blueshift or redshift, depending on the motion of the particle relative to the observer.
105 This effect leads to a Gaussian line shape, with its full width at half maximum (FWHM_D)
106 described in Eq. (3). where M denotes the atomic weight of the absorber.

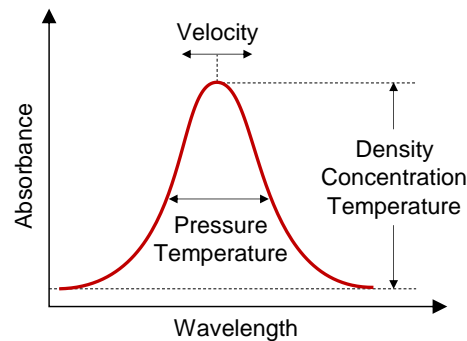
$$107 \quad \text{FWHM}_D(T) = 7.16 \times 10^{-7} \lambda \sqrt{\frac{T}{M}} \quad (3)$$

108 An additional Doppler shift arising from the gas velocity relative to the propagation of light,
109 distinct from thermal Doppler broadening, can induce a spectral shift in the line center. In
110 backscatter measurements, where light enters the vapor cavity against the bulk flow of expelled

111 gases and exits in the same direction, this results in additional line broadening due to the
112 overlap of the red and blue shifts. The nonrelativistic spectral Doppler shift is given by Eq. (4).

113
$$\lambda_{\text{obs}} = \lambda \sqrt{\frac{1 + \frac{v}{c}}{1 - \frac{v}{c}}} \quad (4)$$

114 As illustrated in Fig. 2, the observed absorbance depends on several factors including the
115 number density of the absorber, absorption path length, and gas density or pressure. The
116 resulting line shape function ϕ from Doppler and pressure broadening is a convolution of the
117 Gaussian and Lorentzian profiles, commonly referred to as the Voigt profile [21]. While it is
118 challenging to isolate each of these effects for quantitative measurements, especially in the
119 backscatter configuration where strong gradients may exist, the signal is significantly influenced
120 by gas properties, providing a means for process monitoring or control.



121
122 Fig. 2: Effects of gas properties on the spectral profile of atomic transitions under conditions
123 relevant to metal PBF.

124 3. Experiment

125 3.1. Optical testbed

126 The testbed shown in Fig. 3a is designed to provide optical access to a stationary melt pool and
127 vapor plume under conditions similar to L-PBF and EB-PBF. It consists of a process laser
128 mounted on top of a vacuum chamber. While the process beam is static, the sample, in the form
129 of a solid Ti-6Al-4V metal disk, is mounted on a rotating and translating motion stage to simulate
130 the motion of the process beam scanning over the powder bed. The chamber is connected to a
131 vacuum roughing pump and an Ar gas cylinder allowing the chamber pressure to be adjusted
132 between 0.1–760 Torr. The vacuum chamber has various ports that can be equipped with
133 optical windows.

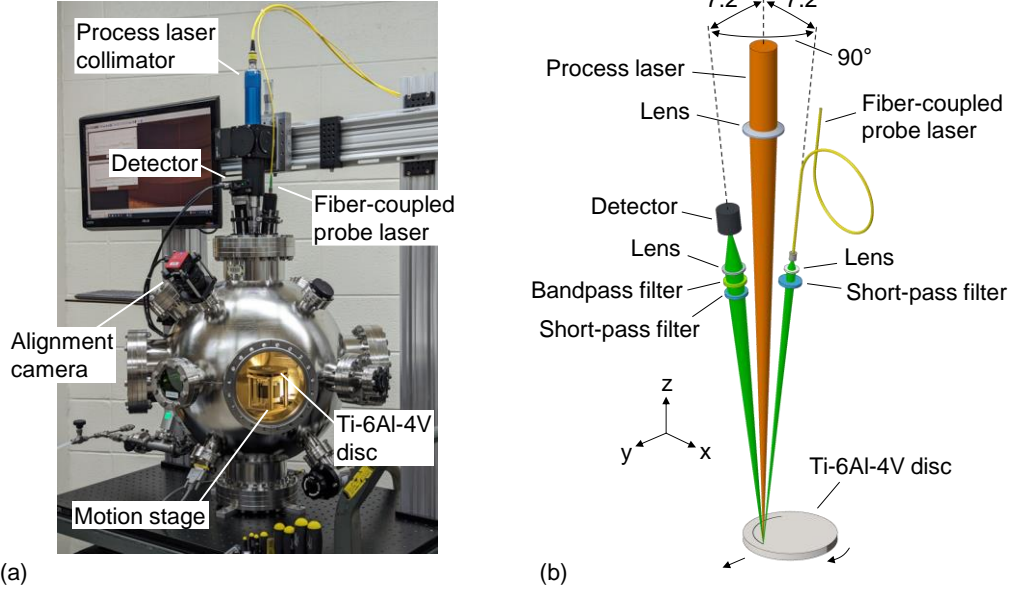


Fig. 3: (a) The optical testbed and (b) the optical arrangement for the BTLAS approach.

As shown in Fig. 3b, the process laser, a Yb:YAG fiber laser (IPG Photonics YLR, $\lambda_p = 1070$ nm, 500 W, beam quality $M_q^2 = 5.9$; IPG P30 collimator: $f = 40$ mm, $d_0 = 20$ mm exit beam diameter), was focused on the sample disk with a focal length $f_i = 500$ mm lens. The $1/e^2$ spot size calculated using Eq. (5) is $d_s \sim 200$ μ m.

$$d_s = \frac{4f_i\lambda_p M_q^2}{\pi d_0} \quad (5)$$

The top flange of the chamber has viewports that provide optical access nearly coaxial with the process laser, with an offset of $\sim 7.2^\circ$ from the process laser axis. This angle was the smallest achievable considering the space required for the windows and optics on the top flange. One window is used for the probe laser, which is delivered via a single-mode optical fiber (see Section 3.2 for details) and focused on the melt pool using an $f = 11$ mm aspheric lens with focus adjustment (Thorlabs CFC11A-A), resulting in a spot size of ~ 200 μ m similar to the process laser. Adjacent to this is a detector (variable-gain Si photodiode, Thorlabs PDA100A2) that captures the backscattered probe laser light through an $f = 40$ mm lens. There is a 90° offset between the illumination and detection ports to reduce the amount of specular reflected light reaching the detector and causing intermittent saturation. Both viewports are equipped with fused silica windows with a 30-arcmin wedge to prevent etalon effects caused by interference from light partially reflected within the glass. Short-pass filters (Thorlabs FESH1000, 1000 nm cut-off wavelength) are used to protect the fiber and detector from backscattered process laser light. In front of the detector, a narrow bandpass filter matching the probe laser wavelength (see

155 Section 3.3 for details) further suppresses the process laser light and blocks blackbody radiation
156 from the melt pool and the vapor plume. With a combined optical density at process laser
157 wavelength of 13.5, both filters effectively eliminate the influence of the process laser on the
158 signal. All lenses and windows are anti-reflective coated for the appropriate wavelength. Unless
159 otherwise stated, the optics are made of BK7 glass.

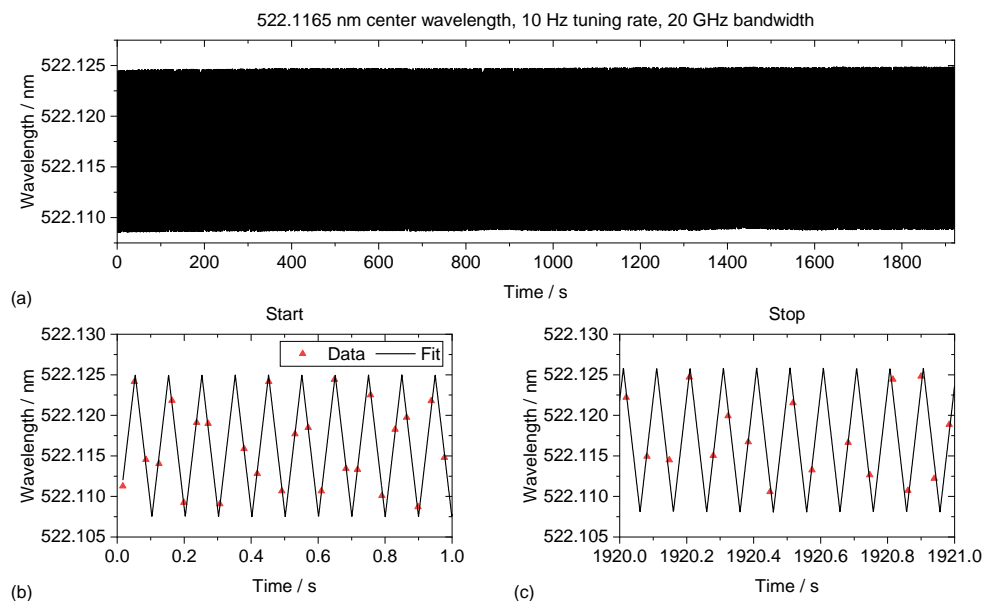
160 A camera (35 $\mu\text{m}/\text{pixel}$ resolution) mounted on one of the 45° ports (Fig. 3a) was used for
161 process monitoring and alignment of the laser beams. To align the beams, the process laser is
162 first used to mark a spot on the metal disk. The probe beam is then adjusted until it aligns with
163 the mark using knobs on a kinematic mount that holds the fiber and optics to the top flange of
164 the vacuum chamber.

165 3.2. Probe laser

166 The probe laser used in this experiment was a commercial visible laser configured in a sum
167 frequency generation (SFG) arrangement (M Squared SolS TiS and EMM, 515–661 nm). A
168 narrow-linewidth Ti:sapphire lasing cavity first produces light between 700–1000 nm, which is
169 then coaligned with a 1950-nm fiber laser and mixed inside a periodically-poled lithium niobate
170 (PPLN) crystal. This setup allows for the modulation of the output wavelength over picometers.
171 The generated visible light was coupled into a single mode optical fiber that delivered it to the
172 optical test bed. The optical power at the fiber output was measured to be approximately 10 mW
173 (Thorlabs PM160 power meter). For all absorption measurements in this paper, the tuning
174 bandwidth was set to 20 GHz, corresponding to a tuning range of 18.2 pm at 522 nm. The
175 tuning rate was set to 10 Hz, i.e., the frequency at which the wavelength is modulated from the
176 lowest to the highest wavelength and back.

177 To evaluate the wavelength tuning stability, the output of the laser system was monitored with
178 wavemeter (HighFinesse WS6-600, 600 MHz accuracy) over a time span of 30 min while the
179 laser was tuned (Fig. 4). Since the sampling rate of the wavemeter was limited to 25 Hz, the
180 tuning rate and range were determined by fitting a symmetrical sawtooth function to the under-
181 sampled data for small time windows of 10 wavelength sweeps each, as shown in Figs. 4a and
182 4b. The resulting tuning rate from the individual fits averaged 10.000 Hz over the whole dataset
183 with a standard deviation of 0.0016 Hz, while the tuning range was 17.3 pm with a standard
184 deviation of 0.32 pm, slightly less than the target tuning range. However, the tuning rate was
185 also observed to vary between measurement days. Since the experimental setup did not allow
186 simultaneous monitoring of the laser wavelength with the wavemeter during the experiments,

187 the authors decided not to derive a wavelength axis from the time trace. Consequently, all
188 signals in Section 4 are presented as a function of time instead of wavelength.



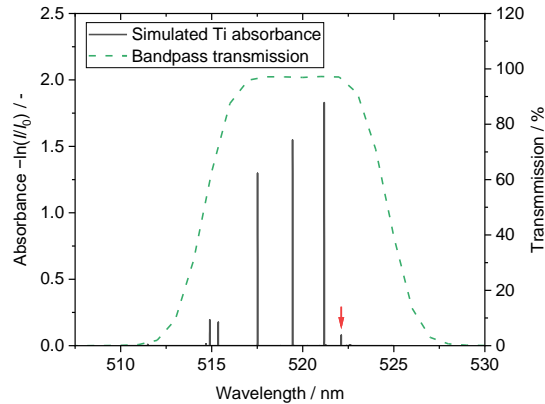
189
190 Fig. 4: Long-term spectral measurement characterizing the laser scanning method. The full
191 trace (a) shows the overall stability and consistency despite undersampling, as demonstrated by
192 cuts in the scan starting (b) and stopping (c) periods.

193 It is important to note that the probe laser power is more than four orders of magnitude lower
194 than the process laser powers used in this work, so the influence of the probe beam on the melt
195 pool is negligible.

196 3.3. Line selection

197 Using the gas temperature reported in previous studies [13,14], spectral simulations were
198 performed (Fig. 5) to identify candidate Ti absorption lines within the spectral range accessible
199 by the probe laser (see Ref. [14] for details on the simulations). Since pressure, absorption path
200 length, and Ti concentration are largely unknown at this point and were therefore arbitrarily
201 chosen for the simulations, the optical bandpass (Thorlabs FBH520-10, 520 nm central
202 wavelength, 10 nm bandwidth) was chosen to accommodate multiple Ti lines with significantly
203 different absorption (dashed green line in Fig. 5).

204 Initial tests (not shown) showed that the absorption of the stronger lines was too strong, causing
205 the plume to be completely opaque. Therefore, the weakest line within this range at 522.155 nm
206 ($3d^24s^2 a^3F_3 \rightarrow 3d^2(^3F)4s4p(^3P^o) z^3F^o_2$ [22], red arrow in Fig. 5) was selected for all
207 absorption measurements.

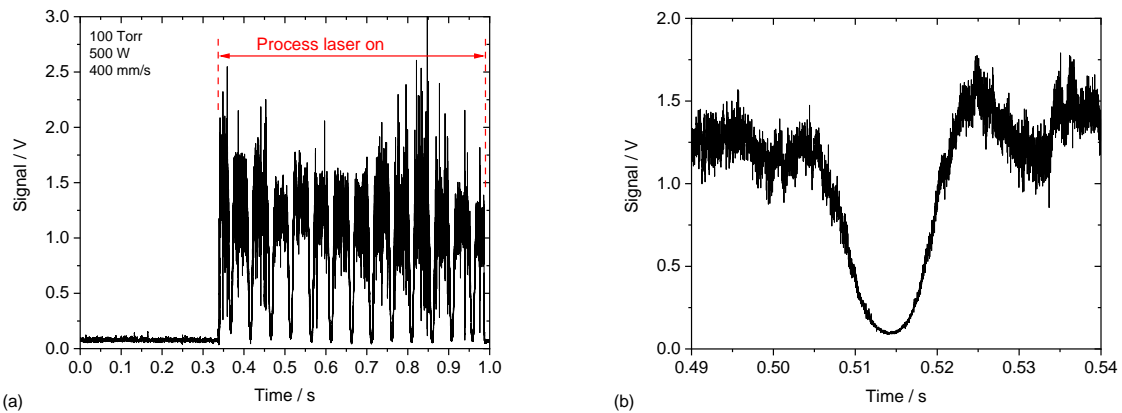


208
 209 Fig. 5: Simulation of Ti absorption assuming a temperature of 3000 K at quasi-vacuum pressure
 210 for an absorption path length of 200 μm (see Ref. [14] for details) along with the bandpass
 211 transmission curve. The red arrow marks the line selected for the experiments presented in the
 212 next section unless stated otherwise.

213 4. Results

214 For each measurement sequence, the Ti-6Al-4V disk was accelerated to reach the desired
 215 speed (400 mm/s unless stated otherwise) at the process beam location. The process laser was
 216 then activated for the full rotation of the sample disk. During the entire run-up and measurement
 217 sequence, the probe laser was active and tuned over the target absorption line, while data
 218 acquisition (National Instruments PXIe-1062Q and PXI-5105) was triggered just before the
 219 process laser was activated. The hatch distance between two consecutive scans was 0.2 mm.

220 Figure 6 shows the raw signal recorded during a measurement sequence. As soon as the
 221 process laser is triggered, the signal level increases significantly. This is consistent with the
 222 backscattered light becoming more directional: as the vapor cavity forms, the beam angle is
 223 expected to become smaller because the light escapes mainly upward through the aperture
 224 after multiple reflections from the walls of the vapor cavity [23]. As a result, more light reaches
 225 the nearly coaxial detector.



226

227 Fig. 6 (a) the raw signal versus time curve recorded at a laser power of 500 W at a scan speed
 228 of 400 mm/s in a 100-torr Ar atmosphere and (b) the same curve zoomed in on a single
 229 wavelength sweep of the probe laser across the Ti spectral line.

230 The intensity and shape of the recorded signal has been found to depend significantly on the
 231 process parameters applied to the signal, as described in the following sections.

232 4.1. Signal intensity

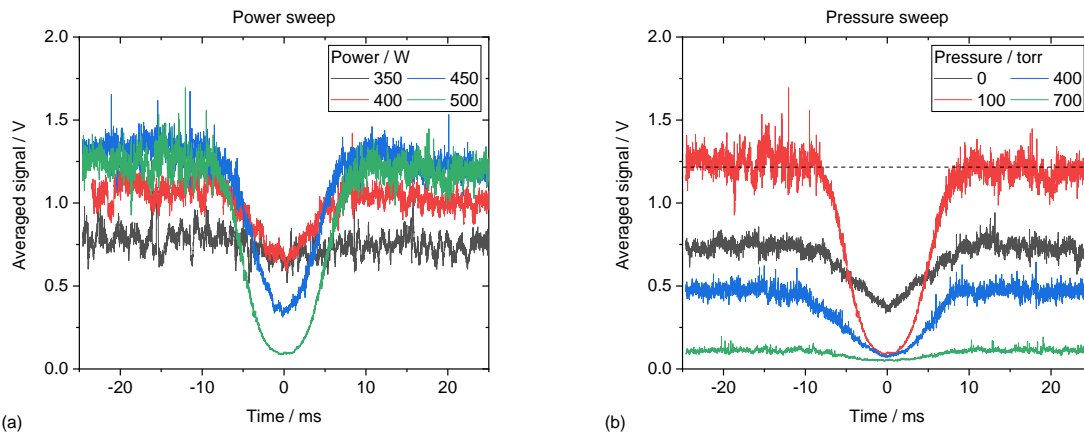
233 The intensity of the backscattered signal depends on the attenuation of the probe laser light due
 234 to absorption at the melt surface and the angle at which it is reflected depending on the shape
 235 of the vapor cavity, which depends on the processing parameters. During the experiments, the
 236 process laser power and the test chamber Ar pressure were varied. Figure 7 shows the signal
 237 ensemble-averaged over six scans for different process laser powers (a) and pressures (b).
 238 Here, the x-axis represents the time relative to the time at which the peak absorbance of each of
 239 the six scans is observed.

240 The probe laser signal level increases with process laser power at a constant pressure of
 241 100 Torr. This can be explained by the increasing depth of the vapor cavity with increasing laser
 242 power, resulting in more directed backscatter [23], and, therefore, more light reaching the
 243 detector.

244 With increasing pressure, however, first an increase of the signal level between 0.1–100 Torr
 245 can be observed before it drops between 100–700 Torr. This is consistent with the simulations
 246 by Li et al. [24] who observed a shallow and round vapor cavity at 10 mbar as the vapor jet is
 247 expelled at a large divergence angle in the low-pressure environment. With increasing chamber
 248 pressure, their simulations show that the vapor cavity becomes initially steeper and deeper
 249 before it becomes shallower again at significantly higher pressure. This could be caused by the

250 reduced recoil pressure as the pressure difference between the vapor cavity pressure and the
251 chamber pressure decreases.

252 Another explanation for the drop at higher pressure could be plasma shielding from partial
253 ionization of the metal vapor, as the temperature in the vapor cavity increases with chamber
254 pressure due to the higher boiling point of the metals at elevated pressure. However, as pointed
255 out by Hanemann et al. [25], the laser fluence at L-PBF is probably insufficient for ionizing the
256 gases. Further, the authors did not observe any optical emission from ionized Ti during this
257 study (see Section 4.4 for emission spectra) and never observed ion emission during initial
258 testing of the optical testbed with a high-resolution spectrometer (not shown).



259 (a) 259
260 Fig. 7: BTLAS signal at 400 mm/s scan speed for varying process laser power at 100 Torr (a)
261 and test chamber pressure at 500 W (b). The plots shown were averaged over six consecutive
262 laser sweeps to reduce noise.

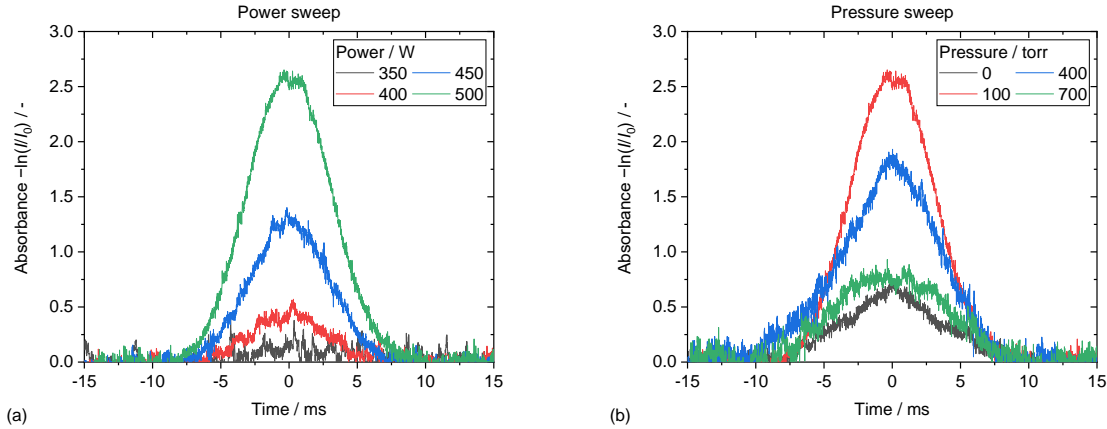
263 4.2. Absorbance

264 The absorbance is calculated using Eq. (1) using the averaged signal (Fig. 7) as I , whereas I_0 is
265 determined by fitting a horizontal baseline to the data trace (dashed line in Fig. 7b). This
266 baseline correction makes the calculation of the absorbance independent of the overall signal
267 intensity.

268 As shown in Fig 8a, the absorbance increases with increasing laser power (Fig. 8a). This trend
269 is consistent with previous findings, where mass loss rates increased with the process beam
270 power [26].

271 For the pressure sweep (Fig. 8b), an initial increase in absorbance is observed from 0.1–
272 100 Torr, which then decreases between 100–700 Torr. The authors attribute this behavior to
273 two competing effects: As the boiling point shifts to higher temperature with increasing gas

274 pressure, the mass loss rate decreases which leads to a lower absorber concentration. At the
275 same time, however, the increasing pressure also increases the density overall, increasing the
276 absorber number density [24].



277
278 Fig. 8: Absorbance derived from the intensity data in Fig. 7 showing a significant dependence
279 on (a) the process laser power at a constant chamber pressure of 100 Torr and (b) chamber
280 pressure at a constant process laser power of 500 W, both at a scan speed of 400 mm/s.

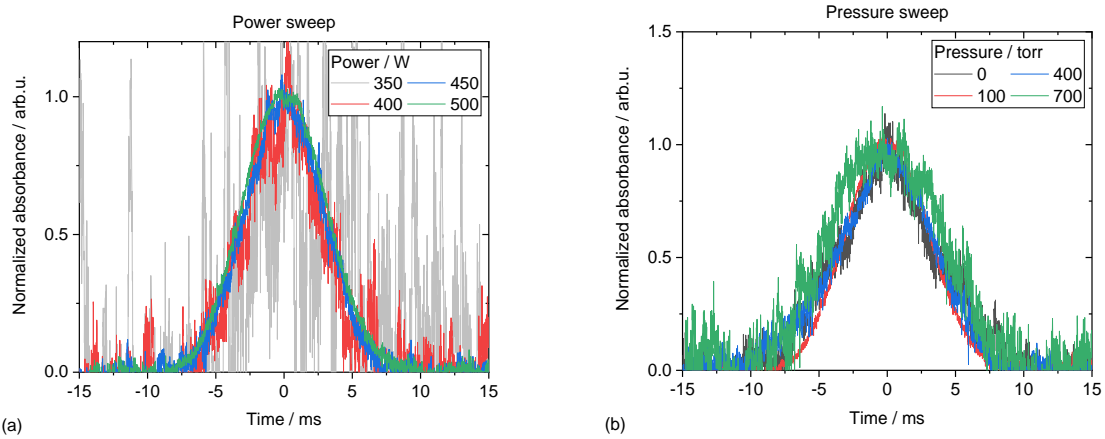
281 4.3. Line shape

282 Variations in line shape are evident when the normalized absorbance is examined (Fig. 8).
283 During the power sweep at 100 Torr (Fig. 9a), the line shape remained invariant, suggesting
284 that the gas temperature remains constant, indicating that evaporation takes place under
285 equilibrium conditions [13].

286 During the pressure variation (Fig. 9a), the Ti line width initially narrows with increasing pressure
287 up to 100 Torr and then broadens again to 700 Torr. This behavior is attributed to the interplay
288 of line-broadening effects: The broadening between 100–700 Torr is consistent with the
289 increased pressure broadening due to the increased chamber pressure. Additionally, increased
290 Doppler broadening occurs due to the rising plume temperature because of the increased
291 boiling point at higher pressures.

292 The initial narrowing between 0 and 100 Torr can be attributed to Doppler shifts (not to be
293 confused with Doppler broadening) because of the increased velocity at which the gas is
294 expelled from the vapor cavity in vacuum: As the probe beam passes through the vapor, first
295 against and then in the direction of flow, the signal undergoes a redshift and a blueshift,
296 respectively. Using the gas velocity of 1500 m/s observed by Li et al. [24] at 10 mbar, the
297 resulting Doppler shift was approximately 2.6 pm (Eq. (4)), which is similar in magnitude to the

298 expected linewidth in vacuum [14]. Since the gas velocity decreases with chamber pressure, the
299 influence of this effect would explain an apparent line narrowing over the 0–100 Torr range.



300
301 Fig. 9: Normalized absorbance during (a) the process laser power sweep at 100 Torr and (b) the
302 pressure sweep at 500 W at a scan speed of 400 mm/s showing differences in line shape
303 depending on the process parameters.

304 It is important to emphasize that the analysis presented in this chapter is largely qualitative, with
305 some speculative elements. To fully discern the interplay of mechanisms affecting line shape
306 and strength, alternative or supplementary measurements and a more comprehensive
307 understanding of the dynamics between gases in the vapor cavity and the melt pool are needed.
308 Nevertheless, the pronounced variability in the observed signals based on processing
309 parameters highlights the potential for advanced process monitoring and closed-loop control,
310 potentially leveraging techniques such as machine learning.

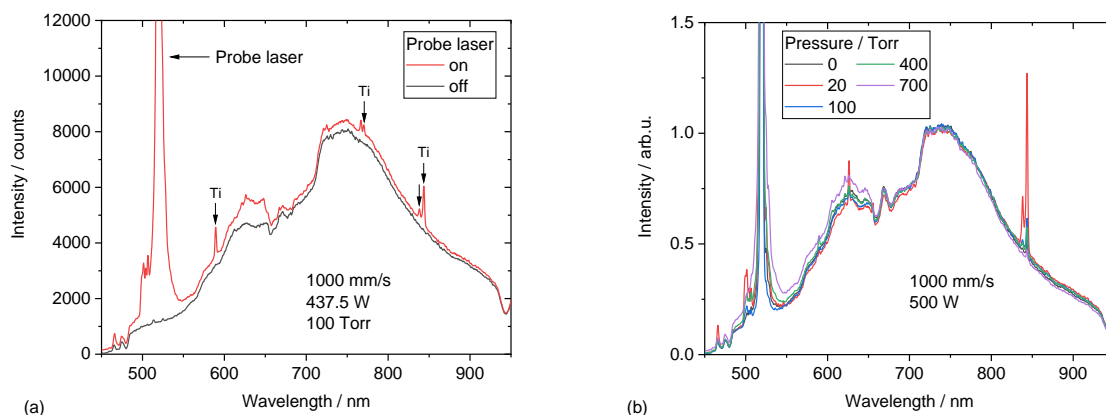
311 4.4. Laser-induced fluorescence

312 The optical emission from the plume was also measured by replacing the detector with an
313 optical fiber (Ocean Optics XSR, 450 μm , 180–800 nm) delivering light to a spectrometer
314 (Optosky ATP2000P, 2.1 nm resolution, 2 ms exposure time). The bandpass filter on the
315 detection side was replaced with a neutral density filter (Thorlabs ND10) to capture light in the
316 visible range without overexposing the spectrometer.

317 Figure 10 shows the plume emission spectrum both without the probe laser and with the probe
318 laser tuned to the stronger 519.442 nm line shown in Fig. 5. In the absence of the probe laser
319 (black curve), no emission lines were visible. However, when the probe laser was on (red
320 curve), Ti lines became clearly visible, suggesting that these lines are due to laser-induced

321 fluorescence (LIF), which is the spontaneous emission of light upon stimulated excitation by
322 absorption of laser light.

323 While there is likely some non-stimulated emission from hot Ti, it is not detectable with the low-
324 resolution spectrometer used in our study. This instrument under-resolves atomic lines by about
325 three orders of magnitude, causing the low-resolution lines to blend into the background signal
326 and become undetectable.



327
328 Fig. 10: (a) Emission spectrum without probe laser and with probe laser tuned to the stronger
329 519.4415-nm absorption line showing laser-induced fluorescence (LIF) and (b) LIF signal for
330 varying chamber pressures at a scan speed of 1000 mm/s.

331 The fluorescence signal varied significantly with chamber pressure, peaking at 20 Torr. This
332 correlates with the observations from the absorbance measurements, where the signal level and
333 absorbance are the highest, while the line width is the lowest at intermediate and low pressures.

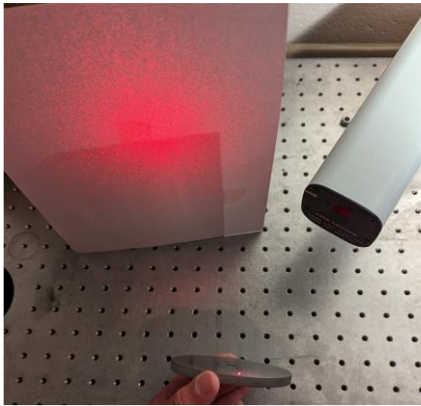
334 5. Discussion

335 5.1. Speckle noise

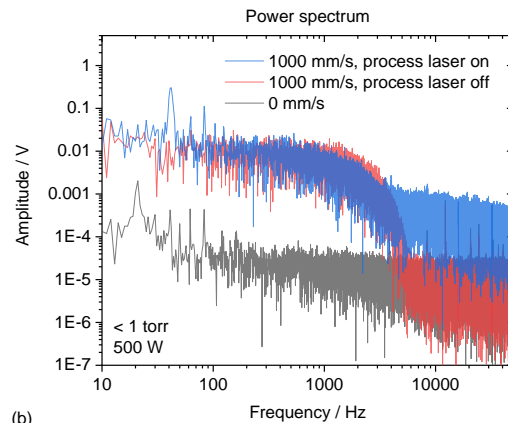
336 The relatively high noise level scales with the signal intensity, indicating that it is caused by
337 speckle noise, which is expected and largely unavoidable. When coherent light is reflected from
338 rough surfaces, speckle patterns, as shown in Fig. 11a, can be observed owing to the
339 interference of the laser light scattered from the high and low points of the rough surface of the
340 illuminated area. The interference pattern changes with the surface speckle, thus changing the
341 signal reaching the detector and resulting in transient noise.

342 Figure 11b shows the Fourier transform power spectrum of the backscattered signal for the
343 stationary sample disk, the moving sample disk, and during an absorption measurement. When

344 comparing the power spectra of the stationary disk with the moving disk, it becomes evident that
 345 the noise caused by motion extends to about 6 kHz. This is similar in magnitude to the speckle
 346 noise frequency of 2.5–25 kHz observed by Wang and Sanders [19] from a rough surface
 347 moving at 300–3000 mm/s. The noise recorded during the absorption measurement extends
 348 beyond the measurement range though also dropping at 6 kHz. This is consistent with recent
 349 research suggesting that keyhole oscillations occur at 40 kHz or faster [27], with the surface
 350 significantly changing several times during each oscillation cycle.



(a)



(b)

351 Fig. 11: (a) Speckle pattern generated by HeNe laser beam scattered off the sample disk
 352 surface; (b) Power spectrum obtained through Fourier transformation of the measured signal,
 353 comparing a stationary disk to a spinning sample disk, both with and without the process laser.
 354

355 To reduce the influence of speckle noise, the laser must be tuned faster than the rate at which
 356 the surface of the melt pool changes. Here, increasing the tuning rate to values well above
 357 6 kHz largely will eliminate the influence of the sample disk motion. To further reduce the
 358 influence of melt pool oscillations, the required tuning rate is likely to be in the range of
 359 hundreds of kilohertz. Such rates have been routinely achieved using, for example, diode lasers
 360 [28,29].

361 Transient speckle noise can also result from tuning the wavelength of the probe beam.
 362 Assuming a typical root mean square (rms) roughness for the powder bed PBF of $h_{rms} = 20 \mu\text{m}$
 363 (Ti-6Al-4V, D50 = 32 μm) [30], the wavelength change needed to alter the speckle pattern is
 364 $\Delta\lambda = \sim 1.5 \text{ nm}$ (Eq. (6)) [19]. Since the probe laser tuning range needed for atomic line
 365 measurements is about 2 orders of magnitude lower (16 pm in this work, see Section 3.2),
 366 speckle noise originating from wavelength tuning can be safely neglected.

367

$$\Delta\lambda = \frac{\lambda^2}{\lambda + 2\sqrt{2}\pi h_{rms}} \quad (6)$$

368 5.2. Representativeness

369 The conditions of the metal vapor in this simplified experiment differ from the still largely
370 unknown conditions in the vapor cavity in L-PBF. The main differences are the larger spot size
371 and slower scan speed compared to most production machines, use of a solid sample instead
372 of metal powder, and the absence of a shielding gas flow. Further work is required to determine
373 whether the technique is applicable to real-world conditions (see Section 6).

374 Furthermore, spatter and ejected powder could be additional sources of scattered light in the
375 L-PBF process. Moreover, the absorption of light by droplets and nanoparticles of condensing
376 metal vapor could be wavelength dependent due to size effects if the particle size is similar to
377 the wavelength of the interrogation laser light. However, these sources of scattered light above
378 the vapor cavity are to some extent out of focus, so that light collection is less efficient, reducing
379 their influence on the overall signal. Further research on the influence of gas-borne particles is
380 needed when applying the BTLAS technique to L-PBF.

381 6. Conclusions and path forward

382 The feasibility of backscatter absorption spectroscopy of gases within the vapor cavity produced
383 during laser processing of solid Ti-6Al-4V was demonstrated. The signal stemming from atomic
384 Ti lines varies significantly with the laser power and build chamber pressure, indicating its
385 potential in process monitoring for quality control or closed-loop feedback in 3D printing.

386 For a practical impact, the technique should be integrated into existing machines and the time
387 resolution should be increased to capture the dynamics of the melt pool/vapor plume
388 interactions. In addition, attempts to mitigate the effects of speckle noise should be pursued. To
389 achieve this, the following steps should be taken.

390 6.1. Application to PBF

391 Before applying the BTLAS technique to production machines, a reasonable next step could be
392 its application to L-PBF or EB-PBF in single-track experiments with metal powders under
393 realistic conditions. For this purpose, the probe beam can be fixed in space while the process
394 beam is scanned across the probe beam spot, similar to previous work studying the metal vapor
395 plume with absorption spectroscopy [12-14]. Here, the ability of single-track testbeds to apply
396 complementary measurement techniques such as X-ray imaging [31,32] can be leveraged to
397 test if and how the BTLAS signal correlates with defects such as pore formation.

398 6.2. Machine integration

399 Coaxial integration is an obvious solution to equip production L-PBF machines with BTLAS
400 sensors. To this end, a dichroic mirror can be placed between the process laser collimator and
401 the galvo mirrors in the scan head. This dichroic mirror would allow process laser light to pass
402 through while reflecting the shorter wavelength of the probe laser. Both incoming and
403 backscattered light would utilize the same pathway with a beam splitter reflecting the light onto
404 the detector.

405 6.3. Multi-line measurements

406 Employing multiple probe beams concurrently can facilitate the targeting of absorption lines
407 from different alloying elements. Signal ratios would then offer insights into the individual mass
408 loss rates of each species. Furthermore, targeting absorption lines with variable temperature
409 dependence could allow quantitative temperature measurements.

410 6.4. Laser-induced fluorescence

411 It should be further explored whether laser-induced fluorescence has potential as a diagnostic
412 tool in additive manufacturing. While high-energy pulsed lasers have been successfully used for
413 LIF experiments in laser welding [33–35], this work showed that relatively low-powered CW
414 lasers can also be used to significantly boost the emission of the vapor plume compared with
415 optical emission spectroscopy of thermally excited metal vapor.

416 6.5. Fundamental research

417 Attention should be paid to determining whether the gas in the vapor cavity comprises neutral
418 atoms or plasma. The authors did not detect any ionized species in this study. Nonetheless, it
419 remains uncertain whether the observed signal decrease at elevated process laser powers and
420 pressures can be attributed to plasma shielding.

421 **Disclosure**

422 During the preparation of this research paper, the authors made use of a combination of
423 generative AI and AI-assisted technologies, specifically DeepL Write, Paperpal, ChatGPT, and
424 Scite. These tools were employed to enhance the quality of the writing, assist in the editing
425 process, and validate citations. Following the use of these tools, the authors carefully reviewed
426 and revised the content as needed and assume full responsibility for the content of the
427 publication.

428 **Author contributions**

429 **M. Beuting:** Conceptualization, Investigation, Formal analysis, Writing - Original draft
430 preparation; **A. J. Fairhall:** Investigation, Formal analysis, Writing - Original draft preparation;
431 **R. H. Goldsmith:** Supervision, Writing - Review & Editing; **L. Chen:** Conceptualization, Funding
432 acquisition, Writing - Review & Editing; **S. T. Sanders:** Conceptualization, Supervision, Writing -
433 Review & Editing

434 **Declaration of interests**

435 A patent application covering the technology described in this manuscript has been filed and is
436 currently pending (application number U.S. 18/231066). There are no other competing interests.

437 **Acknowledgements**

438 This work was supported by the U.S. Department of Commerce (grant number
439 70NANB21H039) and the National Institute of Health (grant number GM-136981). This work
440 was further supported in part by a fellowship award under contract FA9550-21-F-0003 through
441 the National Defense Science and Engineering Graduate (NDSEG) Fellowship Program,
442 sponsored by the Air Force Research Laboratory (AFRL), the Office of Naval Research (ONR)
443 and the Army Research Office (ARO).

444 **7. References**

- 445 [1] P. Yadav, O. Rigo, C. Arvieu, E. Le Guen, E. Lacoste, In Situ Monitoring Systems of The
446 SLM Process: On the Need to Develop Machine Learning Models for Data Processing,
447 Crystals (Basel). 10 (2020) 524. <https://doi.org/10.3390/cryst10060524>.
- 448 [2] M. Wegner, T.S. Hartwich, E. Heyden, L. Schwan, J. Schwenke, N. Wortmann, D. Krause,
449 New Trends in Aviation and Medical Technology Enabled by Additive Manufacturing,
450 Frontiers in Manufacturing Technology. 2 (2022).
451 <https://doi.org/10.3389/fmtec.2022.919738>.
- 452 [3] D. Wang, H. Han, B. Sa, K. Li, J. Yan, J. Zhang, J. Liu, Z. He, N. Wang, M. Yan, A review
453 and a statistical analysis of porosity in metals additively manufactured by laser powder bed
454 fusion, Opto-Electronic Advances. 5 (2022) 210058–210058.
455 <https://doi.org/10.29026/oea.2022.210058>.

- 456 [4] M. Grasso, A. Remani, A. Dickens, B.M. Colosimo, R.K. Leach, In-situ measurement and
457 monitoring methods for metal powder bed fusion: an updated review, *Meas Sci Technol.*
458 32 (2021). <https://doi.org/10.1088/1361-6501/ac0b6b>.
- 459 [5] J. Liu, B. Wei, H. Chang, J. Li, G. Yang, Review of Visual Measurement Methods for Metal
460 Vaporization Processes in Laser Powder Bed Fusion, *Micromachines* (Basel). 14 (2023)
461 1351. <https://doi.org/10.3390/mi14071351>.
- 462 [6] A.A. Martin, N.P. Calta, S.A. Khairallah, J. Wang, P.J. Depond, A.Y. Fong, V. Thampy,
463 G.M. Guss, A.M. Kiss, K.H. Stone, C.J. Tassone, J. Nelson Weker, M.F. Toney, T. van
464 Buuren, M.J. Matthews, Dynamics of pore formation during laser powder bed fusion
465 additive manufacturing, *Nat Commun.* 10 (2019) 1987. [https://doi.org/10.1038/s41467-
466 019-10009-2](https://doi.org/10.1038/s41467-019-10009-2).
- 467 [7] J.A. Kanko, A.P. Sibley, J.M. Fraser, In situ morphology-based defect detection of
468 selective laser melting through inline coherent imaging, *J Mater Process Technol.* 231
469 (2016). <https://doi.org/10.1016/j.jmatprotec.2015.12.024>.
- 470 [8] C.S. Lough, L.I. Escano, M. Qu, C.C. Smith, R.G. Landers, D.A. Bristow, L. Chen, E.C.
471 Kinzel, In-situ optical emission spectroscopy of selective laser melting, *J Manuf Process.*
472 53 (2020). <https://doi.org/10.1016/j.jmapro.2020.02.016>.
- 473 [9] A. R. Ziefuss, R. Streubel, P. Gabriel, F. Eibl, S. Barcikowski, In-situ monitoring of the
474 material composition in PBF-LB via optical emission spectroscopy, *ChemRxiv*. This
475 Content Is a Preprint and Has Not Been Peer-Reviewed. (2023).
- 476 [10] A.J. Dunbar, A.R. Nassar, Assessment of optical emission analysis for in-process
477 monitoring of powder bed fusion additive manufacturing, *Virtual Phys Prototyp.* 13 (2018)
478 14–19. <https://doi.org/10.1080/17452759.2017.1392683>.
- 479 [11] M. Montazeri, R. Yavari, P. Rao, P. Boulware, In-Process Monitoring of Material Cross-
480 Contamination Defects in Laser Powder Bed Fusion, *J Manuf Sci Eng.* 140 (2018).
481 <https://doi.org/10.1115/1.4040543>.
- 482 [12] A. el Farsy, E.C. Tighidet, C. Ballage, T. Minea, Spatiotemporal characterization of
483 evaporated atoms during electron beam melting additive manufacturing by advanced laser
484 diagnostics, *J Appl Phys.* 133 (2023) 044901. <https://doi.org/10.1063/5.0131102>.

- 485 [13] A. el Farsy, V.G. Antunes, B. Seznec, L. Schiesko, C. Ballage, T. Minea, Saturation
486 pressure of nonequilibrium titanium evaporation during additive manufacturing by electron
487 powder bed fusion, *J Appl Phys.* 132 (2022) 054904. <https://doi.org/10.1063/5.0091349>.
- 488 [14] M. Beuting, L.I. Escano, L. Chen, S.T. Sanders, Time-resolved absorption spectroscopy in
489 electron beam melting with blue vertical-cavity surface-emitting lasers, *Opt Express.* 31
490 (2023) 17268. <https://doi.org/10.1364/OE.488551>.
- 491 [15] C.S. Goldenstein, R.M. Spearrin, Jay.B. Jeffries, R.K. Hanson, Infrared laser-absorption
492 sensing for combustion gases, *Prog Energy Combust Sci.* 60 (2017) 132–176.
493 <https://doi.org/10.1016/j.pecs.2016.12.002>.
- 494 [16] C. Liu, L. Xu, Laser absorption spectroscopy for combustion diagnosis in reactive flows: A
495 review, *Appl Spectrosc Rev.* 54 (2019) 1–44.
496 <https://doi.org/10.1080/05704928.2018.1448854>.
- 497 [17] S.T. Melin, Z. Wang, N.J. Neal, D.A. Rothamer, S.T. Sanders, Single-ended retroreflection
498 sensors for absorption spectroscopy in high-temperature environments, *Appl Phys B.* 123
499 (2017) 119. <https://doi.org/10.1007/s00340-017-6687-x>.
- 500 [18] W.Y. Peng, C.S. Goldenstein, R. Mitchell Spearrin, J.B. Jeffries, R.K. Hanson, Single-
501 ended mid-infrared laser-absorption sensor for simultaneous in situ measurements of
502 H₂O, CO₂, CO, and temperature in combustion flows, *Appl Opt.* 55 (2016) 9347.
503 <https://doi.org/10.1364/AO.55.009347>.
- 504 [19] Z. Wang, S.T. Sanders, Toward single-ended absorption spectroscopy probes based on
505 backscattering from rough surfaces: H₂O vapor measurements near 1350 nm, *Appl Phys*
506 *B.* 121 (2015) 187–192. <https://doi.org/10.1007/s00340-015-6216-8>.
- 507 [20] Y. Zhou, G.C. Mathews, C.S. Goldenstein, Compact, fiber-coupled, single-ended laser-
508 absorption-spectroscopy sensors for high-temperature environments, *Appl Opt.* 57 (2018)
509 7117. <https://doi.org/10.1364/ao.57.007117>.
- 510 [21] A.C. Eckbreth, *Laser Diagnostics for Combustion Temperature and Species*, 2nd ed.,
511 Taylor & Francis, New York, NY, 1996.
- 512 [22] A. Kramida, Yu. Ralchenko, J. Reader, NIST ASD Team, NIST Atomic Spectra Database
513 (version 5.9), National Institute of Standards and Technology, Gaithersburg, MD, USA.
514 (2021). <https://physics.nist.gov/asd>.

- 515 [23] B. Lane, I. Zhirnov, S. Mekhontsev, S. Grantham, R. Ricker, S. Rauniyar, K. Chou,
516 Transient Laser Energy Absorption, Co-axial Melt Pool Monitoring, and Relationship to
517 Melt Pool Morphology, *Addit Manuf.* 36 (2020) 101504.
518 <https://doi.org/10.1016/j.addma.2020.101504>.
- 519 [24] X. Li, Q. Guo, L. Chen, W. Tan, Quantitative investigation of gas flow, powder-gas
520 interaction, and powder behavior under different ambient pressure levels in laser powder
521 bed fusion, *Int J Mach Tools Manuf.* 170 (2021).
522 <https://doi.org/10.1016/j.ijmachtools.2021.103797>.
- 523 [25] T. Hanemann, C. Seyfert, P. Holfelder, A. Rota, M. Heilmaier, Dimensionless Enthalpy as
524 Characteristic Factor for Process Control in Laser Powder Bed Fusion, *Journal of Laser
525 Micro/Nanoengineering.* 15 (2020) 257–266. <https://doi.org/10.2961/jlmn.2020.03.2017>.
- 526 [26] D. Deisenroth, S. Mekhontsev, B. Lane, Measurement of mass loss, absorbed energy, and
527 time-resolved reflected power for laser powder bed fusion, in: H. Helvajian, B. Gu, H. Chen
528 (Eds.), *Laser 3D Manufacturing VII*, SPIE, 2020: p. 20.
529 <https://doi.org/10.1117/12.2547491>.
- 530 [27] Z. Ren, L. Gao, S.J. Clark, K. Fezzaa, P. Shevchenko, A. Choi, W. Everhart, A.D. Rollett,
531 L. Chen, T. Sun, Machine learning–aided real-time detection of keyhole pore generation in
532 laser powder bed fusion, *Science* (1979). 379 (2023) 89–94.
533 <https://doi.org/10.1126/science.add4667>.
- 534 [28] A. Farooq, A.B.S. Alquaity, M. Raza, E.F. Nasir, S. Yao, W. Ren, Laser sensors for energy
535 systems and process industries: Perspectives and directions, *Prog Energy Combust Sci.*
536 91 (2022). <https://doi.org/10.1016/j.pecs.2022.100997>.
- 537 [29] A.P. Nair, N.Q. Minesi, C. Jelloian, N.M. Kuenning, R.M. Spearrin, Extended tuning of
538 distributed-feedback lasers in a bias-tee circuit via waveform optimization for MHz-rate
539 absorption spectroscopy, *Meas Sci Technol.* 33 (2022) 105104.
540 <https://doi.org/10.1088/1361-6501/ac7b13>.
- 541 [30] K. Yuasa, M. Tagami, M. Yonehara, T.-T. Ikeshoji, K. Takeshita, H. Aoki, H. Kyogoku,
542 Influences of powder characteristics and recoating conditions on surface morphology of
543 powder bed in metal additive manufacturing, *The International Journal of Advanced
544 Manufacturing Technology.* 115 (2021) 3919–3932. [https://doi.org/10.1007/s00170-021-
545 07359-x](https://doi.org/10.1007/s00170-021-07359-x).

- 546 [31] C. Zhao, K. Fezzaa, R.W. Cunningham, H. Wen, F. De Carlo, L. Chen, A.D. Rollett, T.
547 Sun, Real-time monitoring of laser powder bed fusion process using high-speed X-ray
548 imaging and diffraction, Sci Rep. 7 (2017) 3602. [https://doi.org/10.1038/s41598-017-](https://doi.org/10.1038/s41598-017-03761-2)
549 [03761-2](https://doi.org/10.1038/s41598-017-03761-2).
- 550 [32] C. Ioannidou, H.-H. König, N. Semjatov, U. Ackelid, P. Staron, C. Körner, P. Hedström, G.
551 Lindwall, In-situ synchrotron X-ray analysis of metal Additive Manufacturing: Current state,
552 opportunities and challenges, Mater Des. 219 (2022) 110790.
553 <https://doi.org/10.1016/j.matdes.2022.110790>.
- 554 [33] B.J. Simonds, P. Williams, J. Lehman, Time-resolved detection of vaporization during
555 laser metal processing with laser-induced fluorescence, Procedia CIRP. 74 (2018).
556 <https://doi.org/10.1016/j.procir.2018.08.072>.
- 557 [34] B.J. Simonds, B. Tran, P.A. Williams, In situ monitoring of Cu/Al laser welding using Laser
558 Induced Fluorescence, Procedia CIRP. 94 (2020).
559 <https://doi.org/10.1016/j.procir.2020.09.088>.
- 560 [35] B.J. Simonds, J.W. Sowards, P.A. Williams, Laser-induced fluorescence applied to laser
561 welding of austenitic stainless steel for dilute alloying element detection, J Phys D Appl
562 Phys. 50 (2017). <https://doi.org/10.1088/1361-6463/aa7836>.
- 563